

# <sup>11</sup>C-Acetate PET/CT in Localized Prostate Cancer: A Study with MRI and Histopathologic Correlation

Esther Mena<sup>1</sup>, Baris Turkbey<sup>1</sup>, Haresh Mani<sup>2</sup>, Stephen Adler<sup>1</sup>, Vladimir A. Valera<sup>2</sup>, Marcelino Bernardo<sup>1,3</sup>, Vijay Shah<sup>1,3</sup>, Thomas Pohida<sup>4</sup>, Yolanda McKinney<sup>1</sup>, Gideon Kwarteng<sup>1</sup>, Dagane Daar<sup>1</sup>, Maria L. Lindenberg<sup>1</sup>, Philip Eclarinal<sup>1</sup>, Revia Wade<sup>1</sup>, W. Marston Linehan<sup>5</sup>, Maria J. Merino<sup>2</sup>, Peter A. Pinto<sup>5</sup>, Peter L. Choyke<sup>1</sup>, and Karen A. Kurdziel<sup>1</sup>

<sup>1</sup>Molecular Imaging Program, National Cancer Institute, National Institutes of Health, Bethesda, Maryland; <sup>2</sup>Laboratory of Pathology, National Cancer Institute, National Institutes of Health, Bethesda, Maryland; <sup>3</sup>Imaging Physics, SAIC Frederick, Inc., NCI-Frederick, Frederick, Maryland; <sup>4</sup>Division of Computational Bioscience, Center for Information Technology, National Institutes of Health, Bethesda, Maryland; and <sup>5</sup>Urologic Oncology Branch, National Cancer Institute, National Institutes of Health, Bethesda, Maryland

This work characterizes the uptake of <sup>11</sup>C-acetate in prostate cancer (PCa), benign prostate hyperplasia, and normal prostate tissue in comparison with multiparametric MRI, whole-mount histopathology, and clinical markers to evaluate the potential utility of <sup>11</sup>C-acetate for delineating intraprostatic tumors in a population of patients with localized PCa. **Methods:** Thirty-nine men with presumed localized PCa underwent dynamic–static abdominal–pelvic <sup>11</sup>C-acetate PET/CT for 30 min and 3-T multiparametric MRI before prostatectomy. PET/CT images were registered to MR images using pelvic bones for initial rotation–translation, followed by manual adjustments to account for prostate motion and deformation from the MRI endorectal coil. Whole-mount pathology specimens were sectioned using an MRI-based patient-specific mold resulting in improved registration between the MRI, PET, and pathology. <sup>11</sup>C-acetate PET standardized uptake values were compared with multiparametric MRI and pathology. **Results:** <sup>11</sup>C-acetate uptake was rapid but reversible, peaking at 3–5 min after injection and reaching a relative plateau at approximately 10 min. The average maximum standardized uptake value (10–12 min) of tumors was significantly higher than that of normal prostate tissue ( $4.4 \pm 2.05$  [range, 1.8–9.2] vs.  $2.1 \pm 0.94$  [range, 0.7–3.4], respectively;  $P < 0.001$ ); however, it was not significantly different from that of benign prostatic hyperplasia ( $4.8 \pm 2.01$  [range, 1.8–8.8]). A sector-based comparison with histopathology, including all tumors greater than 0.5 cm, revealed a sensitivity and specificity of 61.6% and 80.0%, respectively, for <sup>11</sup>C-acetate PET/CT and 82.3% and 95.1%, respectively, for MRI. The <sup>11</sup>C-acetate accuracy was comparable to that of MRI when only tumors greater than 0.9 cm were considered. In a small cohort ( $n = 9$ ), <sup>11</sup>C-acetate uptake was independent of fatty acid synthase expression using immunohistochemistry. **Conclusion:** <sup>11</sup>C-acetate PET/CT demonstrates higher uptake in tumor foci than in normal prostate tissue; however, <sup>11</sup>C-acetate uptake in tumors is similar to that in benign prostate hyperplasia nodules. Although <sup>11</sup>C-acetate PET/CT is not likely to have utility

as an independent modality for evaluation of localized PCa, the high uptake in tumors may make it useful for monitoring focal therapy when tissue damage after therapy may limit anatomic imaging methods.

**Key Words:** prostate cancer; <sup>11</sup>C-acetate PET; multiparametric prostate MRI

**J Nucl Med 2012; 53:1–8**

DOI: 10.2967/jnumed.111.096032

**P**rostate cancer (PCa) is the most frequently diagnosed cancer in men and is the second most common cause of cancer death in men in developed countries (1). Early detection of PCa is important because cancer confined to the prostate gland is often curable. However, overtreatment is a concern because many of these cancers are not life-threatening. Prostate-sparing, image-guided therapies for localized PCa are under development in the hope of reducing the morbidities associated with whole-gland radiotherapy or radical prostatectomy. For such focal therapies to become accepted, accurate imaging methods of delineating PCa must be developed.

The ability to image localized PCa remains limited. When PCa is suspected because of high prostate-specific antigen (PSA) or abnormal findings on digital rectal examination, the diagnosis of PCa typically relies on masked, systemic biopsies obtained under ultrasound guidance. Ultrasound has limited sensitivity for PCa and is used primarily to guide the needle to predefined regions of the prostate gland (left and right, apex, mid, and base) without knowledge of the actual location of the cancer.

MRI is the best available imaging technique for identifying PCa. Although T2-weighted (T2W) imaging has been the mainstay of prostate MRI, it is generally nonspecific for cancer, with low signal intensity being associated with prostatitis, scarring, or hyperplasia. Multiparametric MRI has become popular, complementing T2W images with diffusion-weighted imaging, dynamic contrast-enhanced

Received Jul. 21, 2011; revision accepted Nov. 29, 2011.

For correspondence or reprints contact: Karen A. Kurdziel, Molecular Imaging Program, National Cancer Institute, 10 Center Dr., MSC 1182, Bldg. 10, Room B3B69, Bethesda, MD 20892-1088.

E-mail: karen.kurdziel@nih.gov

Published online ■■■■

COPYRIGHT © 2012 by the Society of Nuclear Medicine, Inc.

(DCE) imaging, and MR spectroscopy imaging (MRSI) to improve diagnostic accuracy. Multiparametric MRI remains imperfect, with sensitivities and specificities ranging from 22%–85% to 50%–99%, depending on technical factors and the composition of the study population (2).

Therefore, there is still a compelling need to more accurately identify PCa. PET has emerged as a promising imaging tool for cancer. However, the most commonly used PET radiotracer,  $^{18}\text{F}$ -FDG, has limited sensitivity for PCa (3,4) due to low glucose consumption in early PCa, compounded by artifacts created from high bladder activity (5,6). Preliminary studies have demonstrated promising results with the PET agent  $^{11}\text{C}$ -acetate for the diagnosis of recurrent (7,8) or metastatic PCa (9), but its role in primary PCa detection and staging is less well established (10).

Acetate is a naturally occurring fatty acid precursor that is converted to acetyl-CoA, a substrate for the tricarboxylic acid cycle. Acetyl-CoA is incorporated into cholesterol and fatty acids, and therefore  $^{11}\text{C}$ -acetate uptake is an indirect biomarker of fatty acid synthesis. Data suggest that  $^{11}\text{C}$ -acetate PET/CT is useful in malignancies (11), including PCa (12,13). It has been suggested that because PCa relies more on fatty acid metabolism than on glycolysis (14),  $^{11}\text{C}$ -acetate may be a more appropriate imaging agent than  $^{18}\text{F}$ -FDG (15). Additionally,  $^{11}\text{C}$ -acetate shows minimal bladder activity.

We compared  $^{11}\text{C}$ -acetate PET/CT with 3-T multiparametric MRI and whole-mount pathology to characterize  $^{11}\text{C}$ -acetate uptake in prostate tumors, relative to normal tissue and benign lesions, in patients with localized PCa.

## MATERIALS AND METHODS

### Study Design and Patient Population

Our study complied with the Health Insurance Portability and Accountability Act and was a prospective, single-institution study approved by the local institutional review board. Inclusion criteria included histologically proven adenocarcinoma of the prostate in patients who were eligible for prostatectomy. Exclusion criteria included contraindications to PET/CT or to MRI, contraindication to endorectal coil placement, prior radiation to the pelvis, and androgen deprivation therapy.

Between 2008 and 2010, 40 patients signed consent forms but only 39 (mean age, 58 y; age range, 44–68 y) underwent  $^{11}\text{C}$ -acetate imaging. One was not imaged because of failed tracer synthesis. Data from the first patient, obtained on an Advance camera (GE Healthcare) using a  $^{68}\text{Ge}$  source transmission scan for attenuation correction, were not evaluable because of inadequate registration between the transmission scan and MRI scan. All patients underwent multiparametric MRI within 6 mo of the  $^{11}\text{C}$ -acetate PET/CT. After imaging, all patients underwent standard-of-care robot-assisted prostatectomy and lymph node dissection. There were 38 evaluable datasets; however, the initial dynamic scans (0–6 min) were not available in 5 patients because of technical difficulties.

### $^{11}\text{C}$ -Acetate PET/CT Protocol

One patient was imaged on an LS Discovery (GE Healthcare) in 2-dimensional acquisition mode, whereas the remaining 37

patients were imaged in 3-dimensional (3D) time-of-flight mode on a Gemini TF (Philips Medical Systems) camera with a spatial resolution of 4.8 mm at the center of the field of view (16). The images were reconstructed using the default row-action maximum-likelihood algorithm iterative reconstruction (ordered-subset expectation maximization for the LS Discovery scanner) (17), with standard corrections for randoms, scatter, attenuation, and normalization.

No specific patient preparation was required.  $^{11}\text{C}$ -acetate synthesis was conducted under investigational new drug no. 102705, using sterile conditions and an automated synthesis apparatus with  $^{11}\text{C}$ -carbon dioxide as a substrate.  $^{11}\text{C}$ -acetate was synthesized by reaction of methylmagnesium bromide with  $^{11}\text{C}$ -carbonyl dioxide in tetrahydrofuran, followed by hydrolysis and purification on small ion-exchange columns (18).

After a low-dose transmission CT scan of the abdomen and pelvis, each patient received an intravenous bolus injection of  $^{11}\text{C}$ -acetate (mean dose, 1,472.6 MBq [39.8 mCi]; range, 1,176.6–2,545.6 MBq [31.8–68.8 mCi]), immediately followed by dynamic PET of the lower pelvis (single bed position) for 6 min. After this, alternating 2-min static images were acquired at the initial bed position and at the contiguously superior bed position (lower abdomen) for the remaining 24 min of the study. Thus, static pelvic images were acquired at approximately 10, 16, 22, and 28 min after injection, and the static lower-abdomen scans were obtained at approximately 7, 13, 19, and 25 min after injection. Vital signs were obtained before  $^{11}\text{C}$ -acetate injection and every 10 min during PET/CT. The patients were queried regarding potential subjective adverse events during the scan and immediately thereafter.

### MRI Protocol

MRI studies were performed using a combination of an endorectal coil (BPX-30; Medrad) and a 16-channel anterior cardiac coil (SENSE Torso/Cardiac 32; Philips) on a 3-T magnet (Achieva; Philips) without prior bowel preparation. The endorectal coil was inserted using a semianesthetic gel (Lidocaine; AstraZeneca), with the patient in the left lateral decubitus position. The balloon surrounding the coil was distended with perfluorocarbon (Fluorinert FC-770; 3M) to a volume of approximately 50 mL to reduce susceptibility artifacts induced by air in the coil's balloon. The protocol included triplanar T2W turbo spin echo MRI, diffusion-weighted MRI, 3D MRSI, axial unenhanced T1-weighted MRI, and axial 3D T1-weighted fast field echo DCE MRI sequences. Sequence parameter details were previously published (19).

### Data Analysis

*Histopathologic Analysis and Image Correlation.* There are inherent difficulties in correlating imaging findings with histopathology. After prostatectomy, the prostate gland may deform, and after fixation, variable shrinkage may occur; therefore, sectioning of the fixed specimen does not necessarily correlate exactly with images in terms of thickness or slicing plane, resulting in slight mismatches between pathology and imaging. We reduced this problem using a customized mold for each patient, which was created before surgery using in vivo MRI as previously described (20). The mold ensured that the specimens were sectioned. After fixation, the gland was sliced from the apex to base, at 6-mm intervals in the axial orientation of the MR image while supported inside a customized mold, as close to the MRI plane as possible, ensuring that the PET and MR images were aligned with whole-

mounted prostate specimens with the highest possible accuracy. Further details regarding whole-mount processing can be found online in the supplemental materials (available online only at <http://jnm.snmjournals.org>).

PET/CT images were registered and fused in the same plane as the MR images using MIM 4.2/5.1 (MIM Software Inc.). The transmission CT image was grossly registered to the MR image, using the pelvic bones for initial rotation–translation. The PET image was then brought into the imaging space of the resultant CT/MR image fusion, yielding registration of the PET/CT and MR images. Manual adjustments were made in the MRI/PET registration to account for prostate motion and deformation due to the MRI endorectal coil.

Only tumors larger than 0.5 cm, which included all dominant tumors, were analyzed. Patients were divided into prognostic groups: low risk, a Gleason score equal to or less than 3 + 4, and high risk, a Gleason score equal to or greater than 4 + 3. Patients were also grouped according to serum PSA: less than 4 ng/mL, between 4 and 10 ng/mL, and higher than 10 ng/mL.

*Immunohistochemistry Analysis for Fatty Acid Synthase.* Immunohistochemistry details are included in the supplemental data.

### Imaging Analysis

*Visual Analysis.* PET/CT images were prospectively assessed by 2 experienced nuclear medicine physicians, and MR images were prospectively assessed by 2 experienced radiologists; neither the physicians nor the radiologists were aware of the other modality and histopathology results.

*Lesion-Based Analysis.* On the PET images, volumes of interest (VOIs) were created in visually identified abnormal foci of  $^{11}\text{C}$ -acetate uptake (greater than adjacent background). A small VOI within a homogeneous region of an iliac vessel was used as the vascular input function. VOIs within a homogeneous portion of muscle and normal prostate were used to create reference tissue time–activity curves. PET data were analyzed quantitatively by calculating the maximum standardized uptake value ( $\text{SUV}_{\text{max}}$ ) for each lesion and mean standardized uptake value ( $\text{SUV}_{\text{mean}}$ ) for the input function and reference tissues and by using the Logan (21) and Patlak (22) reference region–based graphical analyses to assess reversible and irreversible tracer binding, respectively.

On MRI, a visible index lesion was defined as a well-circumscribed round ellipsoid, with low signal intensity on T2W MRI and apparent diffusion coefficient maps of diffusion-weighted MRI (19). 3D MRSI was analyzed by acquiring choline-to-citrate ratios within index lesions. Voxels were considered abnormal when the choline-to-citrate ratio was 3 or more SDs ( $0.13 \pm 0.081$ ) above the mean healthy choline-to-citrate ratio ( $\geq 0.373$ ), based on a previous evaluation of 433 healthy, biopsy-negative voxels from the peripheral zone and 44 additional voxels from biopsy-positive cancers (19). DCE MRI was evaluated subjectively for early and intense enhancement, followed by rapid wash-out, characteristic of PCa (19). The overall sensitivities and specificities reported reflect the qualitative assessment of combined multiparametric MRI readout.

VOIs in tumor-containing and normal prostate tissue were defined using T2W MRI. These MRI VOIs were also applied to the reoriented  $^{11}\text{C}$ -acetate PET/CT images, and  $\text{SUV}_{\text{max}}$  time–activity curves for any lesions seen on MRI, but not on PET, were created.

*Sector-Based Analysis.* Sector-based analysis was also performed, using the MR image as an anatomic map. The prostate

was segmented into 5 levels in the superior–inferior axis, and 4 VOIs (left, right, anterior, and posterior quadrants) were created in each axial plane level, resulting in a total of 20 sectors for each patient.

The sector VOIs were applied to the images, and the previously drawn lesion-based VOIs were overlaid on these 20 sectors using the coregistered MR and PET images (MIM 4.2/5.1).

On the basis of the mutual alignment of the histopathology, MR images, and PET/CT VOIs, each sector was assigned as true-positive, true-negative, false-positive, or false-negative according to pathology results for both MRI and PET/CT interpretations. The tumor focus was considered correlated when it was located either in the same sector as, or a sector immediately adjacent to (neighboring region), the corresponding pathologic sector.

For the MRI analysis, a sector was considered tumor-positive when the whole or any part of the lesion was within the sector. For PET analysis, if a small region of interest composed of the hottest 20% of lesion-defined pixels (using an 80% maximum pixel threshold) spanned multiple sectors, all of the affected sectors were considered positive.

Sensitivity, specificity, and accuracy of MRI and  $^{11}\text{C}$ -acetate PET/CT interpretations with respect to histopathology were calculated.

### Statistical Analysis

$\text{SUV}_{\text{max}}$  measurements of  $^{11}\text{C}$ -acetate PET/CT were obtained in tumor and nontumor regions and compared using a paired 2-sided *t* test. Results were presented as mean  $\pm$  SD (*P* values  $< 0.05$  were considered to represent a significant difference).

The diagnostic accuracy of  $^{11}\text{C}$ -acetate PET/CT in PCa was compared with multiparametric MRI using the sector-based analysis, generating receiver-operating-characteristic curves (plots of  $1 - \text{specificity}$  vs. sensitivity) for both modalities. In addition, the SUV of  $^{11}\text{C}$ -acetate uptake was correlated with histopathologic Gleason score and PSA values, using a Spearman rank correlation.

## RESULTS

### Clinical Findings

The final study population consisted of 38 PCa patients (mean age, 58 y; range, 44–68 y) who underwent radical prostatectomy within a mean of 10.5 d (range, 1–34 d) of  $^{11}\text{C}$ -acetate PET/CT. The mean interval between MRI and prostatectomy was 54 d (range, 2–155 d).  $^{11}\text{C}$ -acetate injections were well tolerated by all patients, with the only reported adverse event recorded being a grade 1 taste disturbance during the infusion in 10 patients, which resolved spontaneously. At the time of  $^{11}\text{C}$ -acetate PET, the mean PSA level was  $7.03 \pm 8.88$  ng/mL, and the range was 1.07 to 53.5 ng/mL. Fifteen patients had a PSA level of less than 4 ng/mL, 19 had a level between 4 and 10 ng/mL, and 5 had a level greater than 10 ng/mL. One hundred sixty-seven tumor foci were histopathologically identified in 38 patients, with 80 of these foci (48%) larger than 0.5 cm. Although 6 patients demonstrated more than one smaller tumor focus ( $< 0.5$  cm) aggregated within the same sector area, such aggregates were not identified on imaging. Gleason scoring of the tumor lesions varied between 3 + 3 and 4 + 5. Thirteen tumors were scored as 3 + 3, 45 as

3 + 4, 4 as 4 + 3, 11 as 4 + 4, and 7 as 4 + 5 when all tumors identified on pathology were considered. All pelvic lymph nodes were negative by clinical imaging criteria. After prostatectomy, microscopic involvement of 1 lymph node was found in 1 patient.

### Diagnostic Accuracy of PET/CT and Multiparametric MRI

**Visual Analysis.** On a per-patient basis,  $^{11}\text{C}$ -acetate PET/CT was positive in at least 1 lesion in 34 of the 38 patients (89%), whereas multiparametric MRI was positive in 37 of the 38 patients (97%).

**Lesion-Based Analysis.** Lesion-based analysis revealed 47 true-positive tumor sites, 17 false-negative sites, and 37 false-positive sites for  $^{11}\text{C}$ -acetate PET, resulting in a sensitivity of 73.4%. For multiparametric MRI, 54 sites were identified as true-positive for tumor, 7 as false-negative, and 3 as false-positive, with a resultant sensitivity of 88.5%. The functional multiparametric MRI modalities DW MRI, DCE MRI, and MRSI revealed sensitivities of 80%, 55%, and 27%, respectively.  $^{11}\text{C}$ -acetate PET/CT identified 5 tumor foci that were not seen with any of the MRI modalities, whereas MRI localized 15 tumor sites that were not identified on  $^{11}\text{C}$ -acetate PET/CT.

**Sector-Based Analysis.** In 20 sectors,  $^{11}\text{C}$ -acetate PET/CT showed a sensitivity, specificity, positive predictive value, and negative predictive value of 61.6%, 80.0%, 56%, and 88%, respectively. On multiparametric MRI, these values were 82.3%, 95.1%, 91%, and 89%, respectively.

In pathologically confirmed tumors with visible  $^{11}\text{C}$ -acetate uptake, the mean tumor volume, measured using a volumetric region of interest on MRI, was larger than in tumors without visible uptake ( $3.1 \pm 4.4$  vs.  $0.6 \pm 0.7$   $\text{cm}^3$ ). This difference was statistically significant ( $P \leq 0.001$ ), although there was overlap between groups. Receiver-operating-characteristic analysis showed the disparity between MRI and  $^{11}\text{C}$ -acetate PET/CT to be less, with improved discrimination for both modalities, for lesions greater than 0.9 cm (Supplemental Fig. 1).

**Quantitative Analysis.** Representative time-activity curves (Fig. 1) showed rapid  $^{11}\text{C}$ -acetate uptake in the prostate, peaking approximately 3–5 min after injection, followed by a relative plateau approximately 10 min after injection. The average  $\text{SUV}_{\text{max}(10-12 \text{ min})}$  of the histopathologically confirmed tumors (Fig. 2) was significantly higher ( $4.4 \pm 2.05$ ; range, 1.8–9.2) than that of normal prostate tissue ( $2.1 \pm 0.943$ ; range, 0.7–3.4) ( $P < 0.0001$ ); however, foci of benign prostatic hyperplasia (BPH) (Fig. 3) also showed high  $^{11}\text{C}$ -acetate uptake (average  $\text{SUV}_{\text{max}}$ ,  $4.8 \pm 2.01$ ; range, 1.8–8.8)—uptake that was not significantly different from that of tumor ( $P = 0.65$ ) (Fig. 4A).

Additionally,  $^{11}\text{C}$ -acetate PET/CT identified 2 foci, with an  $\text{SUV}_{\text{max}}$  of 3.8 and 2.9, shown to be prostatitis on histopathology.

The time-activity curves were evaluated using a graphical analysis for reversible tracers (Logan plot), with the slope

estimating the distribution volume ratio (DVR) (21)—a linear function of receptor availability—and using Patlak graphical analysis for irreversible tracers (22), with the y-intercept representing the tracer influx rate.

The Logan plots became linear at approximately 3 min after injection, consistent with reversible binding (Table 1; [Table 1] Supplemental Fig. 2). The average volume of distribution, representing both specific and nonspecific binding, estimated by the slope of the linear portion of the Logan plot was 3.0 ( $r = 0.999$ ) for the dominant tumors ( $n = 38$ ), 3.4 ( $r = 0.997$ ) for BPH ( $n = 21$ ), and 1.4 ( $r = 0.997$ ) for normal prostate ( $n = 38$ ). Using normal prostate as a reference tissue for tissue-specific binding resulted in a DVR of 2.0 ( $r = 0.999$ ) and 2.3 ( $r = 0.999$ ) for tumor and BPH, respectively. The Patlak plots were not linear, suggesting minimal if any irreversible binding.

### Comparison Between $^{11}\text{C}$ -Acetate Uptake and Clinical Markers

No significant correlation was observed between  $^{11}\text{C}$ -acetate  $\text{SUV}_{\text{max}}$  and serum PSA levels ( $r = -0.128$ ) using Spearman correlation.  $\text{SUV}_{\text{max}}$  did not differ between patients with low or high PSA levels: average  $\text{SUV}_{\text{max}}$  of  $3.7 \pm 2.0$  for PSA level less than 4 ng/mL,  $4.9 \pm 2.3$  for PSA between 4 and 10 ng/mL, and  $5.1 \pm 0.8$  for PSA greater than 10 ng/mL ( $P = 0.407$ ) (Fig. 4B). There was no significant correlation between  $\text{SUV}_{\text{max}}$  and tumor focus Gleason scores ( $r = 0.187$ ). Similarly, no significance was found when the tumors based on Gleason scores 3 + 4 and below (average  $\text{SUV}_{\text{max}}$ ,  $4.2 \pm 1.8$ ) and 4 + 3 and above (average  $\text{SUV}_{\text{max}}$ ,  $4.9 \pm 3$ ) ( $P = 0.55$ ) were grouped (Fig. 4C). Immunohistochemistry analysis for fatty acid synthase revealed no visible difference in staining intensity between tumors with high (visible) and low  $^{11}\text{C}$ -acetate uptake (Supplemental Fig. 3).

### DISCUSSION

Although PCa is a multifocal disease, not all prostate tumors have a poor prognosis, and treatment is dictated by the dominant tumor with the highest clinical grade. If  $^{11}\text{C}$ -acetate PET/CT were able to delineate poorer-prognosis lesions in the setting of localized PCa, perhaps the technique could be used to perform targeted biopsies (rather than sextant standard-of-care biopsies performed currently) or to direct focal therapy. Because organ-sparing approaches are being explored, the challenge of monitoring such therapy after tissue ablation has become more apparent. Availability of a noninvasive specific marker not affected by anatomic distortions would be helpful.

Our study aimed to evaluate the uptake of  $^{11}\text{C}$ -acetate in PCa, BPH, and normal prostate tissue in comparison with multiparametric MRI, whole-mount histopathology, and clinical markers.

In a study of 22 patients with histologically confirmed PCa, Oyama et al. demonstrated the feasibility of using  $^{11}\text{C}$ -acetate PET to visualize primary PCa (8), with positive

[Fig. 1]

[Fig. 4]

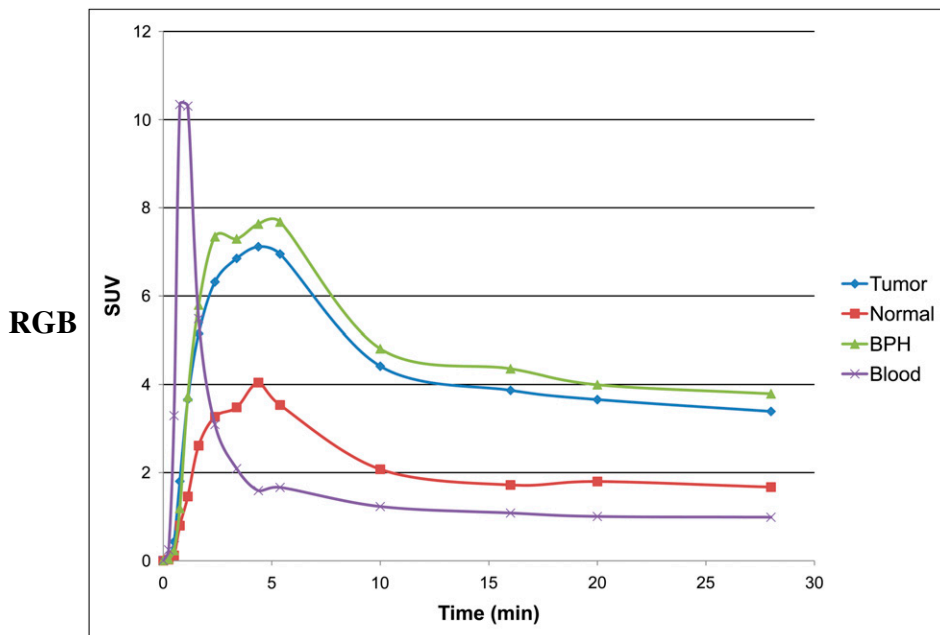


**FIGURE 1.** Time-activity-curve representing mean of all patients, using iliac artery (purple), prostate tumor (blue), BPH foci (green), and normal prostate (red). Uptake is expressed in SUV. Tumor and BPH foci showed rapid uptake of  $^{11}\text{C}$ -acetate in prostate, peaking at approximately 3–5 min, followed by relative plateau after 10 min.

accumulation occurring in all primary tumors, albeit with variable SUVs (3.3–10), on static images obtained 10–20 min after injection. Because only the known tumors were evaluated, their study did not include data on  $^{11}\text{C}$ -acetate uptake in benign prostate conditions, and the PET region of interest was based on visual analysis. Similar results were published by Kato et al. (23), who reported lower but overlapping SUVs for BPH (mean SUV,  $2.1 \pm 0.6$ ) and for prostate tumors (mean SUV,  $1.9 \pm 0.6$ ); however, not all tumors, and none of the BPH foci, had histologic confirmation (23). Their SUVs (measured between 16 and 20 min after injection) in tumor foci were lower than those in our study, likely because of the use of different region-of-interest or data analysis methods. Tumor sizes were not provided in either study.

For our primary analysis, we considered only foci that were greater than 0.5 cm (within the spatial resolution of all imaging systems used) on pathology ( $n = 80$ ), and we reported  $\text{SUV}_{\text{max}}$  determined at the beginning of the uptake plateau: between 10 and 12 min after injection. Our results showed  $^{11}\text{C}$ -acetate uptake to be equal between benign and malignant processes. The  $\text{SUV}_{\text{max}(10-12 \text{ min})}$  of histopathologically defined tumors ranged from 1.8 to 9.2, with an average value of  $4.4 \pm 2.0$ , overlapping that of BPH nodules (mean,  $4.8 \pm 2.0$ ; range, 1.8–8.8). The mean normal prostate tissue uptake was lower, at  $2.1 \pm 0.9$ .

On a lesion-by-lesion visual analysis,  $^{11}\text{C}$ -acetate PET/CT showed a sensitivity of 73.4%, whereas the sensitivity was 88.5% for multiparametric MRI, 80% for diffusion-weighted imaging, 55% for DCE MRI, and 27% for MRSI, placing  $^{11}\text{C}$ -acetate PET/CT between diffusion-weighted imaging and DCE MRI in relative sensitivity.  $^{11}\text{C}$ -acetate PET/CT identified 5 tumors that MRI did not; however, MRI identified 15 tumors not seen on PET. Sensitivity

and specificity values for  $^{11}\text{C}$ -acetate PET/CT were 61.6% and 80%, respectively, whereas the same values for multiparametric MRI were 82.3% and 95.1%, respectively, using a sector-based analysis for which each lesion was assigned to 1 of 20 anatomically based sectors.  $^{11}\text{C}$ -acetate PET showed 124 false-positive sectors due to its uptake in BPH and 62 false-negative sectors; however, interpreting these foci in light of the MRI findings led to a reclassification of

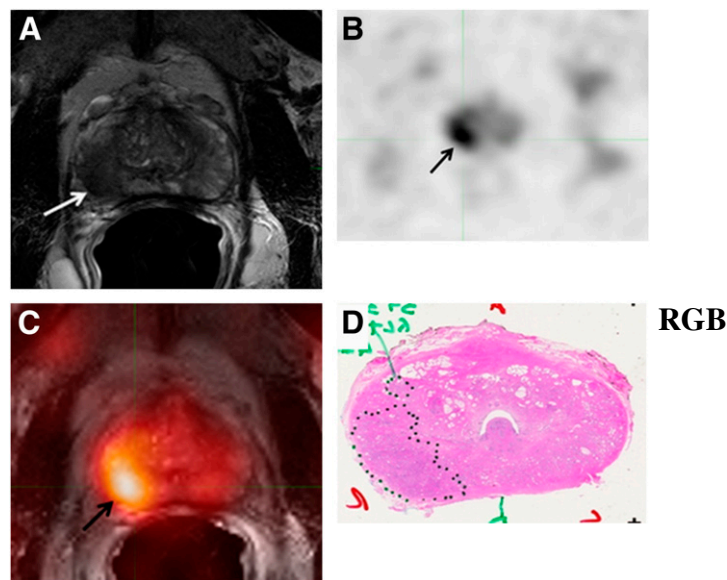


**FIGURE 2.** A 58-y-old man with PCa. Axial T2W MR image (A) demonstrates low-intensity focus in right mid gland peripheral zone (white arrow), which shows  $^{11}\text{C}$ -acetate uptake in axial PET image (black arrow) (B). Fused  $^{11}\text{C}$ -acetate PET/MR image (C) better localizes tumor (black arrow). Corresponding pathology shows Gleason 3 + 4 tumor in right mid peripheral zone (inked in black) (D).

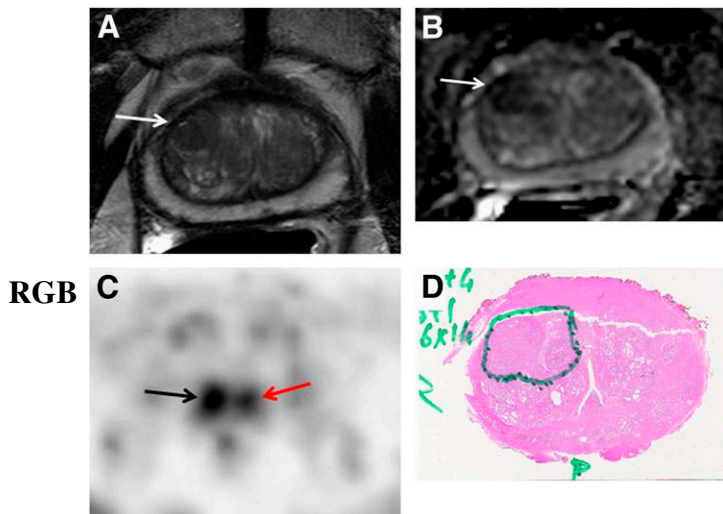


**FIGURE 3.** A 69 y-old-man with PCa. Axial T2W MR image (A) and apparent diffusion coefficient map (B) show low-intensity focus in right mid anterior central gland (white arrows), demonstrating increased  $^{11}\text{C}$ -acetate uptake (black arrow) (C). Corresponding pathology (D) confirms presence of tumor (Gleason 4 + 4), inked in green. Focal  $^{11}\text{C}$ -acetate uptake in left central gland corresponds to BPH nodule (red arrow) (C).

positive PET findings as nonmalignant foci in 30 sites of BPH, which were all confirmed by histopathology.

Both of these analyses demonstrated that  $^{11}\text{C}$ -acetate PET/CT was inferior to multiparametric MRI for lesions greater than 0.5 cm; however, this gap narrowed when only lesions greater than 0.9 cm were considered. The results of the receiver-operating-characteristic analysis showed that both modalities performed better on larger lesions, with sensitivities and specificities of 93.5% (204/218 positive sectors) and 84.9% (477/562 negative sectors), respectively, for MRI and 89.3% (195/218 positive sectors) and 89.9% (505/562 negative sectors), respectively, for PET in lesions greater than 0.9 cm.

As expected, tumors with visible uptake on  $^{11}\text{C}$ -acetate PET/CT were larger ( $3.1 \pm 4.4 \text{ cm}^3$ ) than those without visible uptake ( $0.6 \pm 0.07 \text{ cm}^3$ ;  $P < 0.001$ ). However, the index tumor (largest tumor with the worst Gleason score) is the most significant with regard to progression of PCa, and its response to treatment carries the most clinical importance (24). Although partial-volume correction may have increased the absolute tumor SUVs, it would not have increased their visibility.

Although dynamic uptake of  $^{11}\text{C}$ -acetate in PCa was described by Schiepers et al. (25) in 10 patients and by Kato et al. (23) in 6 patients, neither group compared the results with spatially mapped histopathology. Kato et al. used an early (6–10 min) to late (16–20 min)  $^{11}\text{C}$ -acetate uptake ratio, which was near unity for normal prostate, BPH, and tumor. Schiepers et al. implemented a compartmental model with both bound and free compartments within the prostate and Patlak graphical analysis (assuming irreversible kinetics). Their time–activity curves demonstrated

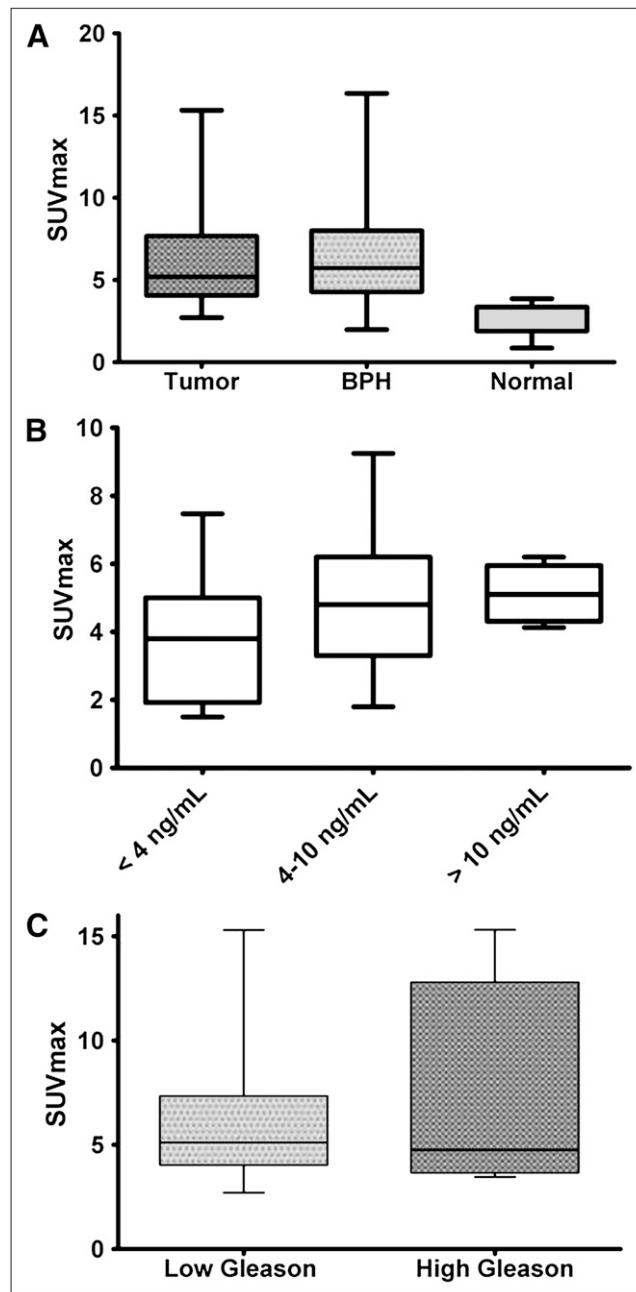


**FIGURE 4.** (A) Prostate tumors and BPH showed similar  $^{11}\text{C}$ -acetate uptake ( $P = 0.757$ ), whereas SUV in normal prostate areas was significantly lower than in tumor ( $P < 0.0001$ ). (B) No significant correlation was noted between SUV and serum PSA levels ( $r = 0.257$ ) or between  $^{11}\text{C}$ -acetate uptake of lesions with lower Gleason scores (3 + 4 and below) and lesions with higher Gleason scores (4 + 3 and above) ( $P = 0.064$ ) (C).

rapid clearance from the blood, with a peak uptake in the prostate tissue at around 5 min, followed by a plateau. This finding is comparable to our results, which show a peak uptake around 3–5 min; however, in our data, this peak is immediately followed by a decrease in activity due to tracer washout just before reaching a plateau. Because the Logan plots became linear at approximately 3 min, indicating equilibrium with blood had been reached, this early peak

**TABLE 1**  
Logan Graphical Analysis Parameters in Tumor, BPH,  
and Normal Prostate

Tissue	Average volume of distribution	DVR
Tumor	3.0 (0.999)	2.0 (0.999)
BPH	3.4 (0.997)	2.3 (0.999)
Normal prostate	1.4 (0.997)	—

*r* values are in parentheses.

was due to initial tumor perfusion. After that peak, our time–activity curves also demonstrate a slow washout of tracer, similar to that of blood clearance, beginning after 10 min. These discrepancies in the time–activity curves, in comparison with previously published results, can probably be explained by the differences in VOI definition; we used the absolute SUV<sub>max</sub> of the VOI defined by the extent of involvement on whole-mount histopathology. Use of the mean SUV would likely have resulted in inclusion of nontumorous tissue because of inherent misregistration. In contrast, without the advantage of PET/CT and registration capabilities, Schiepers et al. (25) used a VOI based on a 50% maximum pixel threshold, which likely included normal prostate tissue, thereby diluting the value (normal prostate SUV and tumor SUV within the VOI). Additionally, they applied partial-volume correction to the input function and not to the tumors. We chose not to apply a partial-volume correction because the size of the lesions and iliac vessels were similar and the corrections would likely have cancelled each other out.

Interestingly, Schiepers et al. (25) reported Patlak graphical analysis parameters for the data between 7 and 20 min (assuming irreversible binding); however, the *K<sub>i</sub>* values (a measure of net tracer flux into the tumor) were quite low and correlation coefficients were not provided. In our data, whereas a relative plateau was reached after 10 min, this was followed by a slow decrease in activity, similar to the blood clearance, suggesting that transfer of tracer from the tumor back to the blood was not negligible and the binding was reversible. Patlak plots of our data were not linear or showed minimally negative slopes. The results of our Logan graphical analysis resulted in excellent linearity (*r* = 0.99). The slope of the Logan plot represents the volume of <sup>11</sup>C-acetate distribution (average volume of distribution) with respect to blood, and these values for tumor, BPH, and normal prostate are listed in Table 1. We also performed a reference tissue–based Logan analysis using the normal prostate as the reference tissue to estimate the DVR between the target lesion and the reference tissue. This value is an indicator of lesion-specific binding (relative to the normal prostate) and eliminates the contribution of the differential organ perfusion and nonspecific binding. The DVR values for tumor and BPH are similar. Although the absolute values of our parameters do not match those of Schiepers et al. (25), a similar uptake in BPH and tumors was found.

Regarding correlation between <sup>11</sup>C-acetate PET and MRI, Jambor et al. (10) found that <sup>11</sup>C-acetate PET/CT detected localized PCa with a sensitivity, specificity, and accuracy of 80%, 29%, and 71%, respectively, comparable to contrast-enhanced MRI. However, neither PET SUVs nor the ratios of MRSI (choline plus creatine plus polyamines) to citrate were included. Oyama et al. (9) found no correlation between clinical parameters and <sup>11</sup>C-acetate uptake.

<sup>11</sup>C-acetate tumor uptake is thought to be due, in part, to increased lipid synthesis. To explore this potential mechanism, we performed immunohistochemistry staining for fatty acid synthase on biopsy samples in a subset of 9 subjects. Levels of staining were high in all tumors, regardless of SUV, indicating that fatty acid synthesis expression is not sufficient to explain the <sup>11</sup>C-acetate mechanism of uptake in humans. This finding is not surprising because previous work from Liu et al. showed a significant overlap of FAS expression in tumor, BPH, and normal prostate (14).

One source of error in our analysis involves our method of image registration. We fused PET, MRI, and histopathology data using a semiautomated mutual information technique, followed by minor manual adjustments. This method introduced a subjective component in accounting for gland deformation. More robust CT-to-MRI deformable registration algorithms are needed to register PET/CT with MRI. Alternatively, the recent development of PET/MRI scanners may obviate registration.

## CONCLUSION

We have characterized the kinetic uptake of <sup>11</sup>C-acetate uptake in tumor, BPH, and normal prostate tissue in localized PCa, with correlation to multiparametric MRI, whole-mount histopathology, fatty acid synthase expression, and clinical markers. <sup>11</sup>C-acetate PET/CT demonstrates higher uptake in intraprostatic tumor foci than in normal prostate tissue; however, uptake in tumors was similar to that in BPH nodules. Although <sup>11</sup>C-acetate PET/CT is not likely to have utility as an independent modality for evaluation of localized PCa, the high differential uptake in tumors, with respect to normal prostate, may make this technique useful for monitoring focal therapy for which posttreatment anatomic changes may limit the utility of MRI.

## DISCLOSURE STATEMENT

The costs of publication of this article were defrayed in part by the payment of page charges. Therefore, and solely to indicate this fact, this article is hereby marked “advertisement” in accordance with 18 USC section 1734.

## ACKNOWLEDGMENTS

We thank Michael Channing and the NIH Clinical Center PET Department for providing the <sup>11</sup>C-acetate. This research was supported by the Intramural Research Program of the NIH, National Cancer Institute, Center for Cancer

Research. No other potential conflict of interest relevant to this article was reported.

## REFERENCES

1. Damber JE, Aus G. Prostate cancer. *Lancet*. 2008;371:1710–1721.
2. Turkbey B, Albert PS, Kurdziel K, Choyke PL. Imaging localized prostate cancer: current approaches and new developments. *AJR*. 2009;192:1471–1480.
3. Liu JJ, Zafar MB, Lai YH, Segall GM, Terris MK. Fluorodeoxyglucose positron emission tomography studies in diagnosis and staging of clinically organ-confined prostate cancer. *Urology*. 2001;57:108–111.
4. Hofer C, Laubenbacher C, Block T, Breul J, Hartung R, Schwaiger M. Fluorine-18-fluorodeoxyglucose positron emission tomography is useless for the detection of local recurrence after radical prostatectomy. *Eur Urol*. 1999;36:31–35.
5. Takahashi N, Inoue T, Lee J, Yamaguchi T, Shizukuishi K. The roles of PET and PET/CT in the diagnosis and management of prostate cancer. *Oncology*. 2007;72:226–233.
6. Schöder H, Larson SM. Positron emission tomography for prostate, bladder, and renal cancer. *Semin Nucl Med*. 2004;34:274–292.
7. Sandblom G, Sorensen J, Lundin N, Haggman M, Malmstrom PU. Positron emission tomography with C11-acetate for tumor detection and localization in patients with prostate-specific antigen relapse after radical prostatectomy. *Urology*. 2006;67:996–1000.
8. Oyama N, Miller TR, Dehdashti F, et al. <sup>11</sup>C-acetate PET imaging of prostate cancer: detection of recurrent disease at PSA relapse. *J Nucl Med*. 2003;44:549–555.
9. Oyama N, Akino H, Kanamaru H, et al. <sup>11</sup>C-acetate PET imaging of prostate cancer. *J Nucl Med*. 2002;43:181–186.
10. Jambor I, Borra R, Kemppainen J, et al. Functional imaging of localized prostate cancer aggressiveness using <sup>11</sup>C-acetate PET/CT and <sup>1</sup>H-MR spectroscopy. *J Nucl Med*. 2010;51:1676–1683.
11. Liu RS. Clinical application of [C-11]acetate in oncology [abstract]. *Clin Positron Imaging*. 2000;3:185.
12. Vävere AL, Kridel SJ, Wheeler FB, Lewis JS. 1-<sup>11</sup>C-acetate as a PET radiopharmaceutical for imaging fatty acid synthase expression in prostate cancer. *J Nucl Med*. 2008;49:327–334.
13. Yoshimoto M, Waki A, Yonekura Y, et al. Characterization of acetate metabolism in tumor cells in relation to cell proliferation: acetate metabolism in tumor cells. *Nucl Med Biol*. 2001;28:117–122.
14. Liu Y. Fatty acid oxidation is a dominant bioenergetic pathway in prostate cancer. *Prostate Cancer Prostatic Dis*. 2006;9:230–234.
15. Shreve P, Chiao PC, Humes HD, Schwaiger M, Gross MD. Carbon-11-acetate PET imaging in renal-disease. *J Nucl Med*. 1995;36:1595–1601.
16. Surti S, Kuhn A, Werner ME, Perkins AE, Kolthammer J, Karp JS. Performance of Philips Gemini TF PET/CT scanner with special consideration for its time-of-flight imaging capabilities. *J Nucl Med*. 2007;48:471–480.
17. Browne J, DePierro AR. A row-action alternative to the EM algorithm for maximizing likelihoods in emission tomography. *IEEE Trans Med Imaging*. 1996;15:687–699.
18. Moerlein SM, Gaehle GG, Welch MJ. Robotic preparation of sodium acetate C 11 injection for use in clinical PET. *Nucl Med Biol*. 2002;29:613–621.
19. Turkbey B, Pinto PA, Mani H, et al. Prostate cancer: value of multiparametric MR imaging at 3 T for detection—histopathologic correlation. *Radiology*. 2010;255:89–99.
20. Shah V, Pohida T, Turkbey B, et al. A method for correlating in vivo prostate magnetic resonance imaging and histopathology using individualized magnetic resonance-based molds. *Rev Sci Instrum*. 2009;80:104301.
21. Logan J, Fowler JS, Volkow ND, Wang GJ, Ding YS, Alexoff DL. Distribution volume ratios without blood sampling from graphical analysis of PET data. *J Cereb Blood Flow Metab*. 1996;16:834–840.
22. Patlak CS, Blasberg RG. Graphical evaluation of blood-to-brain transfer constants from multiple-time uptake data: generalizations. *J Cereb Blood Flow Metab*. 1985;5:584–590.
23. Kato T, Tsukamoto E, Kuge Y, et al. Accumulation of [C-11]acetate in normal prostate and benign prostatic hyperplasia: comparison with prostate cancer. *Eur J Nucl Med Mol Imaging*. 2002;29:1492–1495.
24. Wise AM, Stamey TA, McNeal JE, Clayton JL. Morphologic and clinical significance of multifocal prostate cancers in radical prostatectomy specimens. *Urology*. 2002;60:264–269.
25. Schiepers C, Hoh CK, Nuyts J, et al. 1-<sup>11</sup>C-acetate kinetics of prostate cancer. *J Nucl Med*. 2008;49:206–215.